Low-energy nucleon-nucleus scattering within the energy density functional approach

T. V. Nhan Hao,[1,2,*] Bui Minh Loc,[3,4] and Nguyen Hoang Phuc[3]

[1]*Department of Physics, College of Education, Hue University, 34 Le Loi Street, Hue City, Vietnam*

[2]*Center for Theoretical and Computational Physics, College of Education, Hue University, 34 Le Loi Street, Hue City, Vietnam*

[3]*Institute for Nuclear Science and Technology, VINATOM 179 Hoang Quoc Viet Road, Hanoi, Vietnam*

[4]*University of Pedagogy, Ho Chi Minh City, Vietnam*

(Received 8 March 2015; revised manuscript received 8 May 2015; published 6 July 2015)

The description of nucleons scattering off doubly closed-shell nuclei ^{16}O and ^{208}Pb at energies below 50 MeV is carried out in a fully self-consistent framework of the particle-vibration coupling approach. The applications are performed with commonly used Skyrme-type effective interactions. Nucleon-nucleus optical potentials are thus calculated without ad hoc adjusted parameters. These potentials are then solved with standard optical model codes (DWBA98 in the present case). Empirical nucleon-nucleus elastic angular distributions are thus successfully reproduced.

DOI: 10.1103/PhysRevC.92.014605 PACS number(s): 21.60.Jz, 24.10.Eq, 24.10.Ht, 25.60.Bx

The optical potential (OP) model is a useful tool to study nucleon-nucleus scattering. Most OPs have been generated from phenomenological or microscopic approaches. The phenomenological optical potential (POP) has been obtained by adjustment to the experimental data. It has successfully described nucleon-nucleus (NA) scattering in the mass range $24 \leqslant A \leqslant 209$ with incident energies from 1 keV up to 200 MeV [1]. However, the POP does not have prediction power for the no-experimental region, e.g., the region of neutron-rich exotic nuclei. The microscopic optical potential (MOP) will be a powerful tool to investigate in this region of nuclei. So far, several kinds of approaches for the MOP have been proposed in the literature: so-called nuclear matter approaches [2–4], nuclear structure approaches [5–11], semimicroscopic approaches [12,13], methods based on self-energy theory [14], a method which combines nuclear matter and nuclear structure approaches [16–18], the Faddeev RPA method [19], and the coupled-cluster theory [20]. Nuclear matter approaches [4] could produce satisfactory results at nucleon incident energies $\gtrsim$50 MeV. At energies below 50 MeV, early nuclear structure calculations for NA elastic scattering for heavy-nucleus ^{208}Pb have been performed [7]. This approach only used the Skyrme nucleon-nucleon (NN) effective interaction SIII [21] via the particle-vibration coupling (PVC) method to calculate the OP. Since the absorption part of the OP is too weak, they could not fully explain the observed absorption in nuclear scattering below 30 MeV. Along the same lines, Nobre *et al.* [8,9] provided encouraging results for NA elastic scattering below 70 MeV within the energy density functional structure models. By using the continuum particle-vibration coupling (cPVC) [22] with the SkM* interaction [23], Mizuyama *et al.* [10] have explained 85% of the NA elastic scattering reaction cross section by ^{16}O below 30 MeV. Recently, the energy density functional built from Gogny force has been successfully applied to nucleon-nucleus scattering from ^{40}Ca [11]. However, the nuclear targets of the above nuclear structure approaches (except the calculations of Bernard *et al.* [7]) are limited to the region of light-medium nuclei.

In this paper, we report on the construction of an OP within a fully self-consistent PVC framework. The obtained OP is then applied to describe the NA elastic scattering for light-nucleus ^{16}O and heavynucleus ^{208}Pb at incident energies below 50 MeV.

We start by solving the radial Hartree-Fock (HF) equations in the coordinate space: the radial mesh is 0.1 fm and the maximum value of the radial coordinate is set to be 15 fm. The NN effective interactions SkM* and SLy5 [26] have been adopted. After the HF solutions are found, the ground states and the various excited states are calculated on the basis of the fully self-consistent random phase approximation (RPA) framework as in Ref. [27]. Note that, in contrast to the cRPA calculations performed in Ref. [10], the residual interactions of the RPA method have been fully treated. The continuum has been discretized by adopting the box boundary conditions. To build the particle-hole (p-h) configurations, all the hole states are considered, while for the particle states we choose the eight lowest unoccupied states. In Table I we list the properties of low-lying states in ^{208}Pb. One can see that these states are well described by the RPA calculations. The energy-weighted sum rule for the isoscalar mode of the most collective states such as 3^- (4^+) exhausts 99.50% (99.50%) of the analytic value calculated from the double commutator. After we obtain the RPA excited states, all the natural-parity phonons with multipolarity L from 0 to 5 whose energy is lower than 50 MeV and fraction of the total isoscalar or isovector strength is larger than 5% have been selected for the PVC calculations.

According to Ref. [7], the OP is

$$V_{\rm opt} = V_{\rm HF} + \Delta\Sigma(\omega), \tag{1}$$

where

$$\Delta\Sigma(\omega) = \Sigma(\omega) - \tfrac{1}{2}\Sigma^{(2)}(\omega). \tag{2}$$

In Eqs. (1) and (2), $V_{\rm HF}$ is the local energy-independent HF potential. This potential is the major contribution to the real part of the OP. The locality of $V_{\rm HF}$ is due to the zero-range Skyrme interaction. The polarization potential,

*tran.viet.nhan.hao@gmail.com

TABLE I. Properties of low-lying states in ^{208}Pb obtained by HF-RPA using the SLy5 interaction. Experimental data are taken from [29].

J^π	HF-RPA		Experiment	
	Energy (MeV)	$B(EL,0\to L)$ (e^2 fm^{2L})	Energy (MeV)	$B(EL,0\to L)$ (e^2 fm^{2L})
2_1^+	5.09	3.10×10^3	4.09	3.18×10^3
3_1^-	3.49	6.96×10^5	2.61	6.11×10^5
4_1^+	5.59	1.48×10^7	4.32	1.55×10^7
5_1^-	4.45	5.31×10^8	3.19	4.47×10^8

$\Delta\Sigma$, is nonlocal, complex, and energy dependent. $\Sigma(\omega)$ is the contribution from p-h correlations. $\Sigma^{(2)}(\omega)$ is the second-order potential (SOP) generated from the uncorrelated p-h contribution, and ω is the nucleon incident energy. The factor $\frac{1}{2}$ is added to cancel out the double counting in $\Sigma^{(2)}(\omega)$. It is important to mention that the OP should be nonlocal. The nonlocality of the OP is the consequence of, for example, mapping the effective interactions to the finite-range NNg matrices that are solutions of the Brueckner-Bethe-Goldstone equations for nuclear matter [14,15]. However, the nonlocality of the OP, (1), does not arise from the finite-range character of the interaction since the zero-range Skyrme interaction has been adopted. This is one of the limitations of the present work.

Using the partial wave expansion, the (l,j) components of $\Sigma(\omega)$ are given by

$$\Sigma_{lj}(r,r',\omega)=\hat{j}\sum_{\epsilon_\alpha,\epsilon_\beta}\frac{u_{lj}^{(\epsilon_\alpha)}(r)}{r}\Sigma_{\alpha\beta}^{(lj)}(\omega)\frac{u_{lj}^{(\epsilon_\beta)}(r')}{r'}, \tag{3}$$

where α,β are generic single-particle (s.p.) states, ϵ_i are the s.p. energies, $u_{lj}^{(\epsilon_\alpha)}(r)$ are the radial functions of the s.p. wave functions, and $\hat{j}=(2j+1)^{1/2}$. The sum runs over the complete set of s.p. states. The matrix elements $\Sigma_{\alpha\beta}^{(lj)}(\omega)$ read

$$\Sigma_{\alpha\beta}^{(lj)}(\omega)=\hat{j}_\alpha^{-1}\hat{j}_\beta^{-1}\left(\sum_{nL,A>F}\frac{\langle\alpha||V||A,nL\rangle\langle A,nL||V||\beta\rangle}{\omega-\epsilon_A-\omega_{nL}+i\eta}+\sum_{nL,a<F}\frac{\langle\alpha||V||a,nL\rangle\langle a,nL||V||\beta\rangle}{\omega-\epsilon_a+\omega_{nL}-i\eta}\right), \tag{4}$$

where ω_{nL} are the phonon energies with multipolarity L. a,c,d (A,C,D) denote the hole (particle) s.p. states. Since the s.p. energies are discrete, the fixed parameter $\eta=1.5$ MeV is introduced to perform the energy averaging on the potential $\Delta\Sigma(\omega)$. The reduced matrix elements $\langle i||V||j,nL\rangle$ are calculated as in Refs. [24] and [25]. In the present work, the p-h interaction V has been fully treated.

The calculations of $\Sigma^{(2)}(\omega)$ are similar to that of $\Sigma(\omega)$,

$$\Sigma_{\alpha\beta}^{(2)(lj)}(\omega)=\hat{j}_\alpha^{-1}\hat{j}_\beta^{-1}\left(\sum_{cC,A>F}\frac{\hat{L}^2V_L(\alpha cAC)V_L(\beta cAC)}{\omega-\epsilon_A-(\epsilon_C-\epsilon_c)+i\eta}+\sum_{dD,a<F}\frac{\hat{L}^2V_L(\alpha daD)V_L(\beta daD)}{\omega-\epsilon_a+(\epsilon_D-\epsilon_d)-i\eta}\right), \tag{5}$$

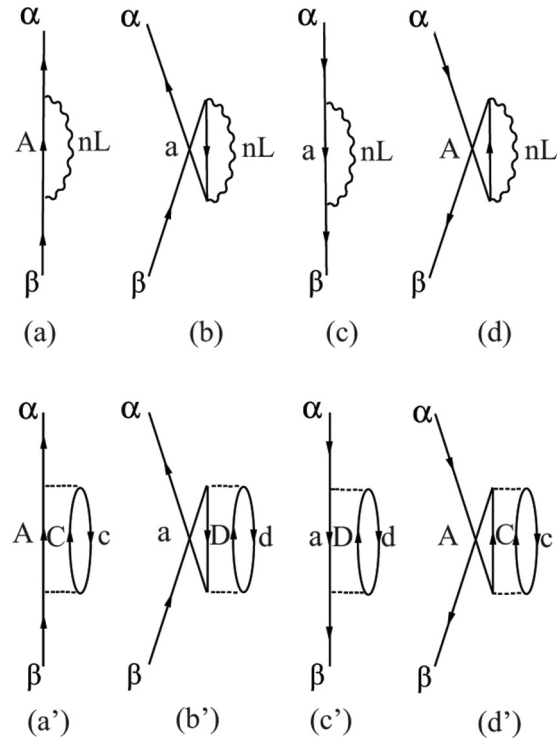

FIG. 1. Diagrammatic representation of the self-energy $\Sigma(\omega)$ and the second-order self-energy $\Sigma^{(2)}(\omega)$. α and β can be either particles or holes.

where $V_L(ihjp)$ are the p-h coupled matrix elements defined in Ref. [24], and $\hat{L}=(2L+1)^{1/2}$. The upper panel (lower panel) in Fig. 1 shows the diagrams associated with the self-energy $\Sigma(\omega)$ [the second-order self-energy $\Sigma^{(2)}(\omega)$]. Figures 1(a) and 1(c) [1(a') and 1(c')] correspond to the direct terms of Eq. (4) [Eq. (5)], whereas Figs. 1(b) and 1(d) [1(b') and 1(d')] correspond to the exchange terms of Eq. (4) [Eq. (5)].

To obtain the observables for the NA elastic scattering, the OP, (1), is used in a nonlocal Schrödinger equation. This equation is solved by the standard DWBA98 code [28]. Note that we do not introduce any local equivalent potential to treat the nonlocality of the OP.

It is of interest to compare the cPVC and PVC methods used to generate the OP. The advantage of the cPVC over the PVC method [7,24,25] is the implementation of proper continuum treatment. The price to be paid is that it is not easy to introduce the corrections for the Pauli principle violated in the underlying cRPA calculations. Therefore, the SOP of the OP has usually been neglected as in Refs. [10] and [22]. In addition, it is well known that the low-lying collective state 4^+ gives the main contribution to the absorption of the OP [7]. However, the properties of this state are not well described by the present cRPA calculations compared with the RPA ones. For example, the cRPA electromagnetic transition probability associated with the first 4^+ state of ^{208}Pb is 0.516×10^7 e^2 fm^8, whereas the same quantity obtained from RPA (extracted from Table I) is 1.480×10^7 e^2 fm^8 (the experimental value is 1.55×10^7 e^2 fm^8 [29]). It should also be mentioned that, due to specific features of the continuum treatment, the whole

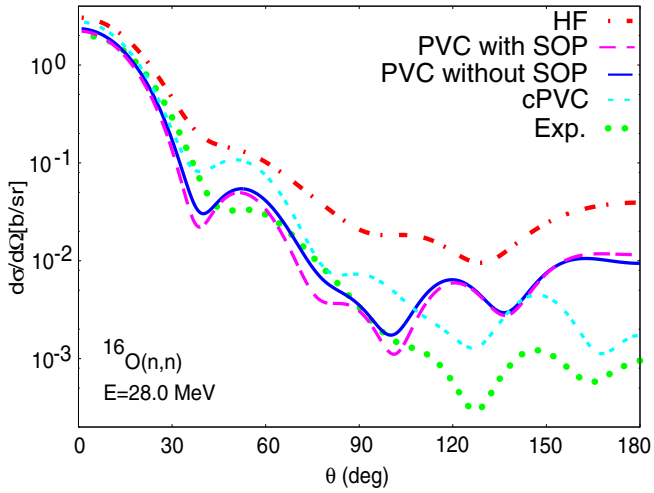

FIG. 2. (Color online) Angular distributions of the neutron elastic scattering by ^{16}O at 28 MeV. The interaction SkM* has been used. The solid (long-dashed) curve shows the results of PVC calculations with (without) the SOP. HF and cPVC results (extracted from Ref. [10]) are denoted by the dot-dashed and short-dashed lines, respectively. Experimental data are taken from Ref. [30].

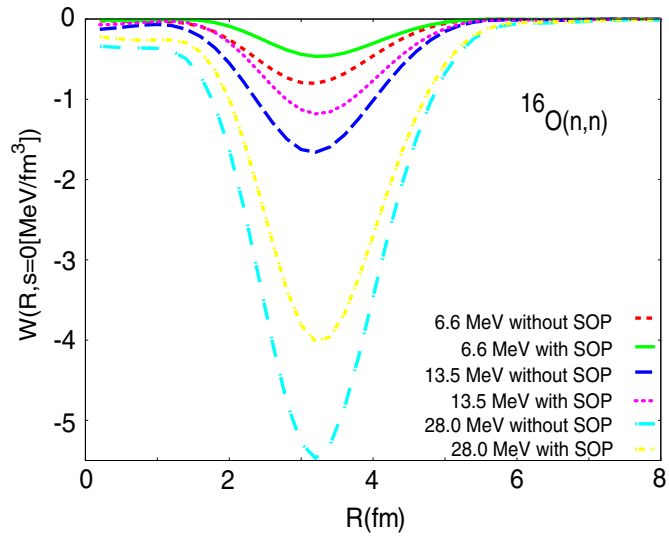

FIG. 3. (Color online) Calculated $W(R,s=0)$ by ^{16}O at different incident energies. The interaction SkM* has been used.

two-body spin-dependent terms, the spin-orbit terms, and the Coulomb term have been dropped in the cRPA as well as in the cPVC calculations. The velocity-dependent part of the p-h interaction of the cPVC method, which simulates somehow the finite range for the zero-range Skyrme interaction, is approximately treated by the Landau-Migdal approximations (but not in the underlying cRPA method).

To understand more the merits and limitations of the cPVC and PVC methods, the PVC calculations have been performed within the input of the cPVC calculations as in Ref. [10] in order to reproduce the angular distributions of the neutron elastic scattering by ^{16}O at 28 MeV. The interaction SkM* has been adopted. The solid (long-dashed) line in Fig. 2 shows the PVC calculations with (without) the SOP. The HF and cPVC results (extracted from Ref. [10]) are denoted by the dot-dashed and short-dashed lines, respectively. The results show that the PVC with the SOP describes the cross sections better than others at scattering angles smaller than 100°. In the larger-scattering-angle region, the cPVC yields the best agreement with the experimental data. To see the effects of the SOP on the absorption part of the OP, we study the quantity $W(R,s) = \sum_{lj} \frac{2j+1}{4\pi} \mathrm{Im}\Delta\Sigma_{lj}(r,r',\omega)$, where $R = \frac{1}{2}(r+r')$ corresponds to the radius and shape of $\mathrm{Im}\Delta\Sigma$, and $s = r - r'$ shows its nonlocality. The shape of diagonal contributions $W(R,s=0)$ with (without) the SOP at different incident energies are presented in Figs. 3 and 4 by ^{16}O and ^{208}Pb, respectively. In both nuclei, the SOP reduces the strength of $W(R,s=0)$ at the nuclear surface as well as in the interior region. It should be noted that the effect of the SOP increases in nucleon incident energy. For light nuclei, the effect of the SOP is small but it should not be neglected. At an incident energy of 28 MeV, the SOP reduces the reaction cross section of neutron elastic scattering by ^{16}O from 683.12 to 633.33 mb. For heavy nuclei, the SOP could be ignored at incident energies below 15 MeV, whereas the effect of the SOP is very small in the incident energy range 15 MeV $< \omega <$ 50 MeV. Therefore, the results demonstrate that the Pauli blocking effect is more essential in few-body systems than heavy nuclei in the low-incident-energy region, below 50 MeV.

Figure 5 shows the shape of $W(R,s=0)$ for neutron elastic scattering by ^{208}Pb at $E = 14.5$ MeV (solid line). The interaction SLy5 has been used. The result is compared with that of Bernard *et al.* [7] at the same neutron incident energy (dashed line). At the nuclear surface, the absorption of the OP is much stronger since all the terms of the effective interaction have been considered to describe the particle collective state coupling. In the interior region, the weak density-dependent interaction SLy5 (ρ^α with $\alpha = 1/6$) leads to non-null absorption inside. Therefore, the angular distributions

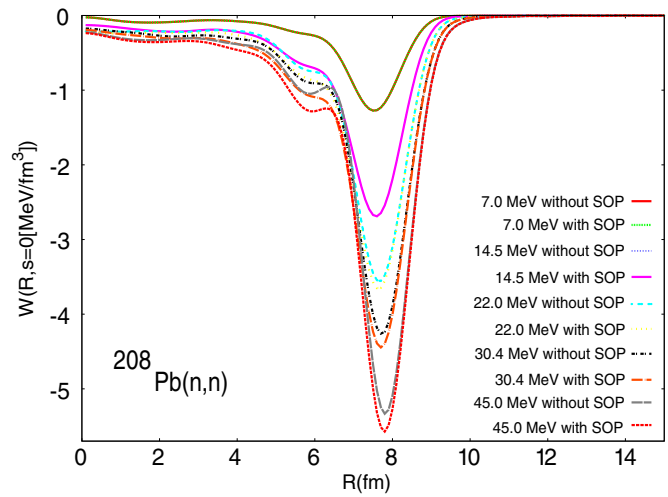

FIG. 4. (Color online) Calculated $W(R,s=0)$ by ^{208}Pb at different incident energies below 50 MeV. The interaction SLy5 has been used.

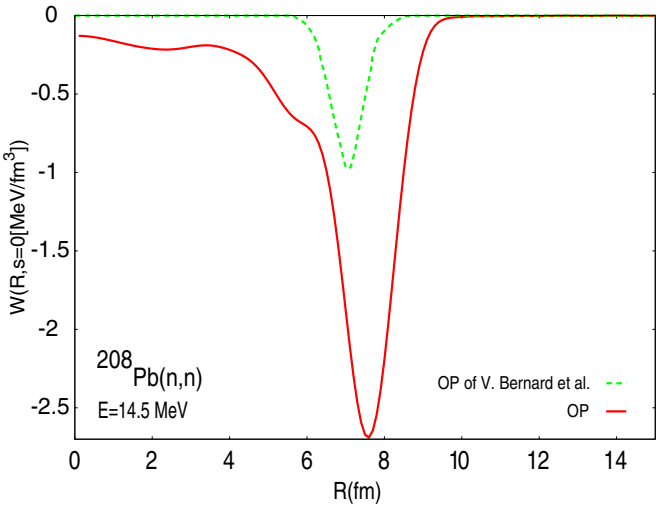

FIG. 5. (Color online) Calculated $W(R,s=0)$ by ^{208}Pb at $E=14.5$ MeV. The interaction SLy5 has been used. The solid line corresponds to OP calculations; the dashed line, to results taken from Ref. [7].

for neutron elastic scattering by ^{208}Pb at $E=14.5$ MeV are successfully reproduced. The result shows the sensitivity of choosing the interactions to the calculations of nuclear reaction observables. Figure 6 shows the contributions of multipole modes to the cross sections at incident energy $E=14.5$ MeV. The results indicate that the main contributions come from the most collective 3^-, 4^+, and 2^+ states, while the 5^- and 1^- states contribute less to the absorption.

In Fig. 7 we show the angular distributions at different incident energies lower than 50 MeV. The experimental data have been well reproduced. The successful differential cross sections in the small-scattering-angle region indicate that

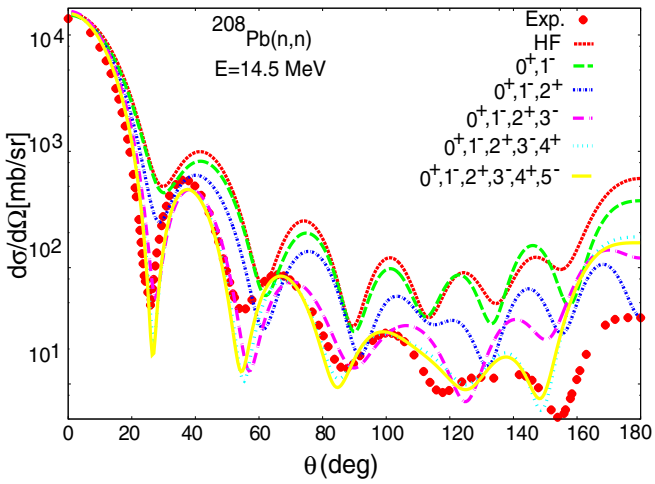

FIG. 6. (Color online) Contributions of the multipole modes to angular distributions of neutron elastic scattering by ^{208}Pb at incident energy $E=14.5$ MeV. The interaction SLy5 has been used. HF results are denoted by the solid line. Short-dashed, dotted, long-dashed, dotted/short-dashed, and dotted/long-dashed lines correspond to calculations with the maximum multipolarity $L_{\max}=1$, 2, 3, 4, and 5, respectively. Experimental points are taken from Ref. [30].

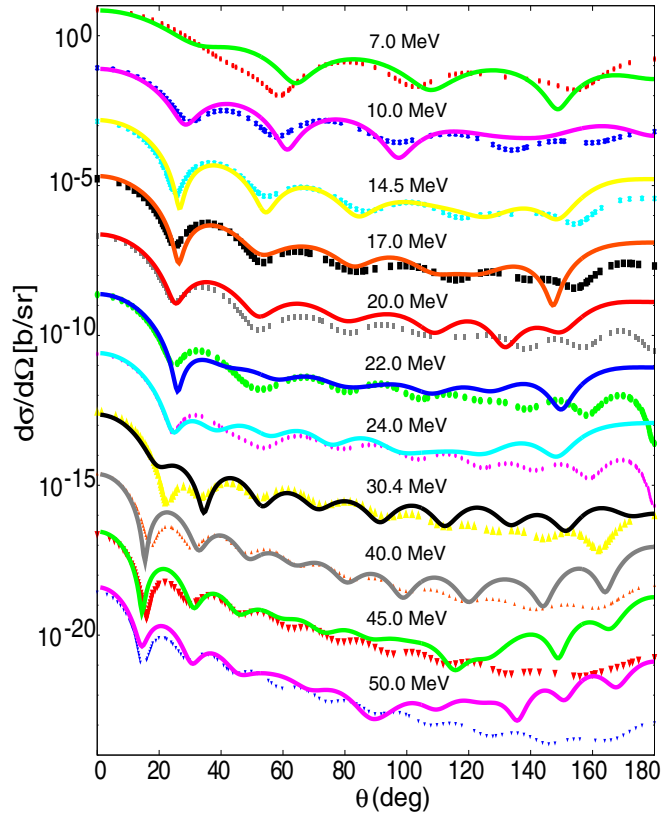

FIG. 7. (Color online) Angular distributions of neutron elastic scattering by ^{208}Pb at different incident energies below 50 MeV. The interaction SLy5 has been used. Solid curves show the results of OP calculations. Experimental points are taken from Ref. [30].

the surface properties of the imaginary part of the OP are satisfactorily described. The disagreement at large scattering angles is due to the lack of absorption in the interior region as well as the incorrect real part of the OP.

We have used the nuclear structure approach to reproduce the angular distributions data of the neutron elastic scattering at incident energies below 50 MeV. The investigation of the proton elastic scattering could be performed without difficulties. In this model, the calculations of nuclear reactions observables directly depend on the nuclear structure inputs adopted, especially on the effective interaction. Therefore, this model is useful for the parametrization process of new variants of the effective Skyrme-type interaction which could simultaneously describe the nuclear structure and nuclear reactions. At low incident energies, the work presented here could be a simple and feasible tool for experimentalists not only to analyze scattering data but also to interpret the resulting analysis.

The authors are grateful for the support of N. Van Giai, D. T. Khoa, G. Colò, L.-G. Cao, and K. Mizuyama. T.V.N.H. thanks the Service Informatique de IPN Orsay for the excellent working conditions provided to him and the France Vietnam Particle Physics Laboratory (FV-PPL LIA) for the partial support. This research is funded by the Vietnam National Foundation for Science and Technology Development (NAFOSTED) under Grant No. 103.04-2013.07.

[1] A. J. Koning and J. P. Delaroche, Nucl. Phys. A **713**, 231 (2003).
[2] J.-P. Jeukenne, A. Lejeune, and C. Mahaux, Phys. Rev. C **16**, 80 (1977).
[3] C. Barbieri and B. K. Jennings, Phys. Rev. C **72**, 014613 (2005).
[4] M. Dupuis, S. Karataglidis, E. Bauge, J. P. Delaroche, and D. Gogny, Phys. Rev. C **73**, 014605 (2006).
[5] N. Vinh Mau, *Theory of Nuclear Structure* (IAEA, Vienna, 1970), p. 931.
[6] N. Vinh Mau and A. Bouyssy, Nucl. Phys. A **257**, 189 (1976).
[7] V. Bernard and N. Van Giai, Nucl. Phys. A **327**, 397 (1979).
[8] G. P. A. Nobre, F. S. Dietrich, J. E. Escher, I. J. Thompson, M. Dupuis, J. Terasaki, and J. Engel, Phys. Rev. Lett. **105**, 202502 (2010).
[9] G. P. A. Nobre, F. S. Dietrich, J. E. Escher, I. J. Thompson, M. Dupuis, J. Terasaki, and J. Engel, Phys. Rev. C **84**, 064609 (2011).
[10] K. Mizuyama and K. Ogata, Phys. Rev. C **86**, 041603(R) (2012).
[11] G. Blanchon, M. Dupuis, H. F. Arellano, and N. Vinh Mau, Phys. Rev. C **91**, 014612 (2015).
[12] E. Bauge, J. P. Delaroche, and M. Girod, Phys. Rev. C **58**, 1118 (1998).
[13] E. Bauge, J. P. Delaroche, and M. Girod, Phys. Rev. C **63**, 024607 (2001).
[14] K. Amos, P. J. Dortmans, H. V. von Geramb, S. Karataglidis, and J. Raynal, *Advances in Nuclear Physics* (Plenum Press, New York, 2000), Vol. 25, p. 275.
[15] P. K. Deb, K. Amos, S. Karataglidis, M. B. Chadwick, and D. G. Madland, Phys. Rev. Lett. **86**, 3248 (2001).
[16] Q.-b. Shen, Y.-l. Han, and H.-r. Guo, Phys. Rev. C **80**, 024604 (2009).
[17] V. V. Pilipenko, V. I. Kuprikov, and A. P. Soznik, Phys. Rev. C **81**, 044614 (2010).
[18] V. V. Pilipenko and V. I. Kuprikov, Phys. Rev. C **86**, 064613 (2012).
[19] S. J. Waldecker, C. Barbieri, and W. H. Dickhoff, Phys. Rev. C **84**, 034616 (2011).
[20] G. Hagen and N. Michel, Phys. Rev. C **86**, 021602(R) (2012).
[21] M. Beiner, H. Flocard, N. Van Giai, and P. Quentin, Nucl. Phys. A **238**, 29 (1975).
[22] K. Mizuyama, G. Colò, and E. Vigezzi, Phys. Rev. C **86**, 034318 (2012).
[23] J. Bartel, P. Quentin, M. Brack, C. Guet, and H. B. Hakansson, Nucl. Phys. A **386**, 79 (1982).
[24] G. Colò, H. Sagawa, and P. F. Bortignon, Phys. Rev. C **82**, 064307 (2010).
[25] L.-G. Cao, G. Colò, H. Sagawa, and P. F. Bortignon, Phys. Rev. C **89**, 044314 (2014).
[26] E. Chabanat, P. Bonche, P. Haensel, J. Meyer, and R. Schaeffer, Nucl. Phys. A **635**, 231 (1998).
[27] G. Colò, L. Cao, N. Van Giai, and L. Capelli, Comput. Phys. Commun. **184**, 142 (2013).
[28] J. Raynal, DWBA98, NEA 1209/05 (1998).
[29] Experimental data taken from the National Nuclear Data Center, Brookhaven National Laboratory Online Data Service; http://www.nndc.bnl.gov/ensdf/
[30] Data retrieved from the National Nuclear Data Center, Brookhaven National Laboratory Online Data Service, http://www.nndc.bnl.gov/exfor/endf00.jsp